Deep convolutional autoencoder for radar-based classification of similar aided and unaided human activities

MEHMET SAYGIN SEYFIOĞLU, Student Member, IEEE
AHMET MURAT ÖZBAYOĞLU, Member, IEEE
TOBB University of Economics and Technology, Ankara, Turkey

SEVGI ZUBEYDE GÜRBÜZ, Senior Member, IEEE
University of Alabama, Tuscaloosa, AL USA

Radar-based activity recognition is a problem that has been of great interest due to applications such as border control and security, pedestrian identification for automotive safety, and remote health monitoring. This paper seeks to show the efficacy of micro-Doppler analysis to distinguish even those gaits whose micro-Doppler signatures are not visually distinguishable. Moreover, a three-layer, deep convolutional autoencoder (CAE) is proposed, which utilizes unsupervised pretraining to initialize the weights in the subsequent convolutional layers. This architecture is shown to be more effective than other deep learning architectures, such as convolutional neural networks and autoencoders, as well as conventional classifiers employing predefined features, such as support vector machines (SVM), random forest, and extreme gradient boosting. Results show the performance of the proposed deep CAE yields a correct classification rate of 94.2% for micro-Doppler signatures of 12 different human activities measured indoors using a 4 GHz continuous wave radar—17.3% improvement over SVM.

Manuscript received April 26, 2017; revised November 5, 2017; released for publication January 9, 2018. Date of publication February 6, 2018; date of current version August 7, 2018.

DOI. No. 10.1109/TAES.2018.2799758

Refereeing to this contribution was handled by A. Charlish.

Authors' addresses: M. S. Seyfioğlu and A. M. Özbayoğlu are with the Department of Electrical and Electronics Engineering, TOBB University of Economics and Technology, Ankara 06510, Turkey, E-mail: (mssey-fioglu@etu.edu.tr; mozbayoglu@etu.edu.tr); S. Z. Gürbüz is with the Department of Electrical and Computer Engineering, University of Alabama, Tuscaloosa, AL 35487, USA, E-mail: (szgurbuz@ua.edu). *(Corresponding author: Sevgi Zubeyde Gürbüz.)*

I. INTRODUCTION

Radar-based human gait recognition has been of great interest due to its relevancy to problems of border control and security [1], [2], pedestrian recognition for automotive safety [3], and fall detection for assisted living [4]. Recently, however, the potential for micro-Doppler analysis to distinguish highly similar human gait has come to attention due to the increasingly smaller size and lower cost of software-defined and wireless radar platforms that are readily available, which have made possible applications of indoor radar. For years, indoor monitoring has been most often accomplished using video surveillance devices; however, in health applications, where privacy both at home and in hospital or assisted living facilities is of paramount importance, radar offers distinct advantages. Radar has the ability to facilitate gait recognition remotely, and in little or no light, without the potential of exposing the human body. Although initial application of radar to assisted living has focused on fall detection [5]–[7], investigation of radar for fall risk assessment and disease monitoring requires the identification of daily indoor activities, which, especially in the case of elderly, often result in highly similar micro-Doppler signatures.

Conventional techniques for micro-Doppler analysis involve first extracting some set of predefined features [8]. These many be physically intuitive features [9], such as Doppler bandwidth and envelope; transform-based computational features, such as discrete cosine coefficients [10] or cepstral coefficients; or speech-processing inspired features, such as mel-frequency cepstral coefficients [11] or linear predictive coding coefficients (LPC) [12]. After dimension reduction or feature selection [13], [14], a fixed set of features is supplied to a classifier, such as support vector machines (SVM), among others, to process a set of test data. Such techniques have been shown in a variety of works [15], [16] to yield high classification performance.

However, as the number and similarity between classes increases, the performance of classifiers using predefined features is significantly degraded [17]. Deep learning, on the other hand, has recently emerged as a powerful technique for classifying imagery, enabled by the immense computational power of modern graphics processing units (GPUs). In one of the first works on radar micro-Doppler classification with deep learning in 2016, Kim and Moon [18] utilized a convolutional neural network (CNN) with 3 convolutional layers and 20 filters to classify 7 different activities: running, walking, walking while holding a stick, crawling, boxing while moving forward, boxing while standing in place, and sitting still. The network was trained in a supervised fashion with 756 spectrogram images, yielding a classification performance of 90.9%—an accuracy that was roughly the same as that previously reported using physical features and SVM [16]. Later, Jokanovic [19] used a two-layer autoencoder (AE) structure with a total of 120 data samples to classify four classes of activities (falling, sitting, bending, and walking) with an accuracy of 87%.

While the spatially localized convolutional filtering of CNN's are advantageous in capturing local features of input images, the neural network is randomly initialized prior to supervised training. As a result, it is possible that the gradient descent process implemented during training may find a less optimal local minimum, depending upon where the initialization began. In contrast, the AE directly learn features from unlabeled data in an unsupervised fashion. Especially in cases when signatures are highly similar, such that a predefined feature set capable of distinguishing classes is not readily apparent, unsupervised pretraining that learns features from the data itself can discover nuances in the data that in fact improves classification performance.

A key challenge in applying deep learning to the classification of radio frequency (RF) signals, however, is the small amount of data available in contrast to the millions of images on the internet that could be used to test deep learning in other fields, such as visual data processing. Thus, another important benefit of unsupervised pretraining is that it effectively functions as a regularizer, preventing the network from potentially overfitting the data [20]. A disadvantage of an AE, however, is that they fail to capture two-dimensional (2-D), spatial variations in the data [21].

This paper proposes the use of a deep three-layer convolutional autoencoder (CAE), which essentially combines the benefits of CNNs and AEs by first using unsupervised pretraining [22] to initialize the network near a good local minima and provide regularization, followed by supervised fine-tuning of the convolutional layers to extract spatially localized features [21], [23]. Moreover, a filter concatenation technique [24] is employed in which different sized filters, namely 3×3 and 9×9, are concatenated to take advantage of multilevel feature extraction. In this paper, the classification performance of the proposed CAE architecture is compared with that attainable using a CNN, an AE, and multi-class SVM for the problem of discriminating 12 classes of aided and unaided indoor human activities, such as potentially encountered in assisted living environments.

In Section II, the experimental test setup and preprocessing steps used to prepare the micro-Doppler dataset used in this study is presented. In Sections III and IV, details on optimal selection of predefined features for SVM, and optimal deep neural network (DNN) architectures are given. In Section V, results for classification performance are compared for each architecture. Finally, in Section VI, important conclusions are discussed.

II. RADAR MICRO-DOPPLER MEASUREMENTS

Radar measurements of human activity were made in an indoor laboratory environment spanning a range of 1–5 m using an NI-USRP 2922 model software-defined radio platform programmed to transmit a continuous wave signal at 4 GHz. Two SAS-571 antennas having a 48° azimuthal beam width were mounted along with the USRP 1 m above the ground. Measurements were taken such that the direction of motion were directly aligned with the center of the antenna beam pattern. Each gait sample was measured separately over a different run to ensure statistical independence in samples. A picture of the radar system is shown in Fig. 1.

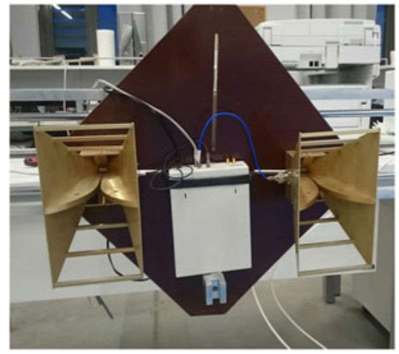

Fig. 1. Configuration of the radar hardware.

A total of 11 different people were used as test subjects to collect 1007 gait samples spanning 12 different classes. Table I summarizes the number of data samples collected per class. The gait for each class was enacted as follows:

1) Walking—medium speed, with fully extended two-arm swing.
2) Jogging—medium speed, two arms held bent at elbows, shortened swing.
3) Limping—left foot dragging on ground behind right foot.
4) Walking with a cane—"candy-cane" style, single-poled, metal cane used to restrict motion of one arm.
5) Walking with walker—two-wheeled, metal walker restricting arm swing of both arms.
6) Walking with crutches—two metal crutches, one leg bent at knee.
7) Crawling—slow advancement on hands and knees.
8) Creeping—military-style motion with belly on ground.
9) Wheelchair—wheels turned manually with both hands.
10) Falling—pretended to "trip" on an object and fall forward onto a mat.
11) Sitting—quick motion to sit on a chair.
12) Falling from chair—falling sideways off chair on to mat.

A. Micro-Doppler Signatures

In this paper, spectrograms were used to represent the time–frequency distribution of the measured micro-Doppler signature. Spectrograms are defined as the modulus of the short-time Fourier transform (STFT)

$$\mathrm{STFT}(m, \omega) = \sum_{n=-\infty}^{\infty} x[n] w[n-m] e^{-j\omega n} \tag{1}$$

where *x[n]* is the received signal and *w[m]* is a window function. In this paper, a hamming window with length of 2048 samples, 4096 fast Fourier transform (FFT) points, and 128 samples overlap were utilized. Each spectrogram was then cropped to a duration of 4 s, converted to gray scale, normalized between 0 and 1 and saved as an image. To reduce dimensionality, the resulting images were then

TABLE I
Number of Samples Per Class (F.C. denotes falling from chair)

Class	Walking	Jogging	Crawling	Limping	Cane	Falling	Wheelchair	Crutches	Sitting	Walker	F.C.	Creeping
Samples	71	72	74	104	123	53	149	74	50	121	60	56

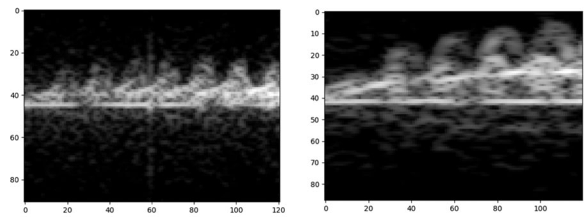

(a) (b)

Fig. 2. SMOTE-generated synthetic spectrograms: (a) walking and (b) jogging.

down-sampled from a size of 656 × 875 pixels to 90 × 120 pixels.

B. Mitigating Effects of Class Imbalance

One issue with dataset generation that is frequently overlooked is class imbalance. It is quite common, due to practical constraints on collecting data from multiple subjects, that the number of data samples for each class are not equal. Imbalance in the dataset can cause algorithms to be biased toward the classes having more data. Although the imbalance of 3:1 in this dataset is not as severe as that seen in other applications, such as 100:1 or even 100 000:1, rather than truncating the data to achieve balance, in this paper, the synthetic minority oversampling technique (SMOTE) [25], [26] is applied on the training dataset to prevent imbalanced learning and avoid overfitting. The SMOTE algorithm equalizes class data by oversampling minority classes with "synthetic" samples. First, the pixels of the 2-D spectrogram are converted into a concatenated one-dimensional vector. Then, the synthetic samples are generated by taking the difference between the sample under consideration and its nearest neighbor. This difference is multiplied by a random number between 0 and 1, and added to the sample under consideration. This procedure can be generalized for k-nearest neighbors and N% oversampling. For example, consider a case where five-nearest neighbors are used for 200% oversampling. Two of the five-nearest neighbors are chosen and random samples are generated in the direction of each nearest neighbor selected. The SMOTE algorithm was used in conjunction with tenfold cross validation by first randomly selecting 90% of the data for training and the remaining 10% for testing. The SMOTE algorithm is then applied on the training data only, using five-nearest neighbors and varying the amount of oversampling so as to equalize the number samples in each class. Only real, measured data is used in the testing process. Fig. 2 shows two examples of SMOTE-generated synthetic spectrograms for walking and jogging, which may be compared to the measured spectrograms for each class shown in Fig. 3.

III. CLASSIFICATION WITH PREDEFINED FEATURES

One of the most often used methods in the literature for the classification of micro-Doppler signatures is classification with predefined features—features that are extracted through a fixed computation process. A plethora of features [8] have been defined in the literature, including physical, transform-based, and speech-processing inspired features. A wide range of these features is considered in this paper, as defined next.

A. Feature Definitions

Physical features are direct measurements of properties of the spectrogram or cadence velocity diagram (CVD) and relate to human gait parameters. The CVD [27]–[29] is defined as the Fourier transform of the spectrogram along each frequency bin

$$\Delta(v, \omega) = \left| \sum_{n=0}^{N-1} \mathrm{STFT}(n, \omega) e^{\frac{-j2\pi n v}{N}} \right| \tag{2}$$

and provides a measure of how often the different velocities repeat (i.e., cadence frequencies). The 13 physical features utilized in this paper are as follows:

1) bandwidth of torso response;
2) mean of the torso response;
3) minimum value of the upper envelope;
4) maximum value of the upper envelope;
5) mean value of the upper envelope;
6) minimum value of the lower envelope;
7) maximum value of the lower envelope;
8) mean value of the lower envelope;
9) overall Doppler bandwidth,
10) difference between upper and lower envelope averages,
11) gait frequency, i.e., fundamental frequency of CVD,
12) second harmonic of CVD,
13) third harmonic of CVD.

Transform-based features, as computed from the first ten coefficients of the discrete-cosine transform (DCT) of the micro-Doppler frequency, $x[n]$, as

$$C[k] = h[k] \sum_{t=0}^{T-1} x[n] \cos\left[\pi \left(n + \frac{1}{2}\right) \frac{k}{T}\right] \tag{3}$$

where T is the length of the observed radar signature, $k \in [0, n-1]$, and $h[k]$ is defined as

$$h[k] = \begin{cases} \sqrt{\frac{1}{T}} & \text{for } k = 0 \\ \sqrt{\frac{2}{T}} & \text{otherwise.} \end{cases} \tag{4}$$

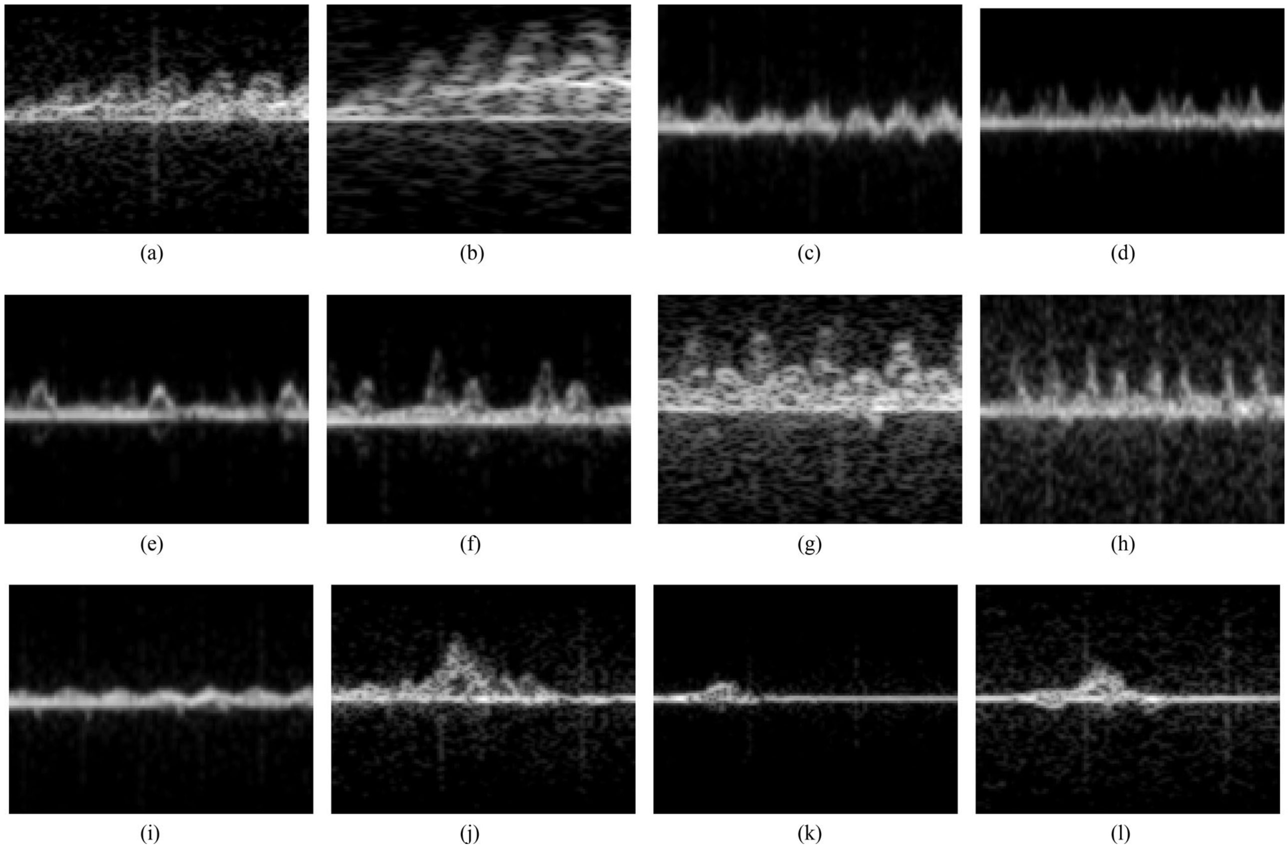

Fig. 3. Examples of measured spectrograms for each human activity class: (a) walking, (b) jogging, (c) limping, (d) walking with cane, (e) walking with walker, (f) walking with crutches, (g) crawling, (h) creeping, (i) wheelchair, (j) falling, (k) sitting, (l) falling from chair.

Along with the first three cepstral coefficients, and 101 LPC are also used as features in this paper. LPC and cepstral coefficients are features originally proposed in speech processing literature, but which have also found utility in micro-Doppler analysis. LPC's are computed by representing this signal as the linear combination of past values

$$\hat{x} = \sum_{k=1}^{p} a[k]x[n-k] \tag{5}$$

where $a[k]$ are the LPCs and p is the total number of LPCs. To compute the LPCs, the difference between the model in (5) and the true signal—i.e., the error $e[n] = x[n] - \hat{x}[n]$—is sought to be minimized. Many methods can be employed for this minimization, such as computing the autocorrelation followed by a Levinson–Durbin recursion.

The cepstrum, $c[n]$, is defined as the inverse DFT of the log magnitude of the DFT of the received radar return $x[n]$

$$c[n] = F^{-1}[\log|F[x[n]]|] \tag{6}$$

where $F[.]$ is the Fourier transform.

To summarize, a total of 127 features is extracted: 10 DCT, 3 cepstral, 13 physical, and 101 LPC.

B. Feature Selection and Classifier Comparison

Due to the curse of dimensionality, utilizing all possible features does not necessarily guarantee the greatest performance. Dimension reduction [30] and feature selection [8], [13], [31] methods have been shown to yield significant improvements in classification accuracy. In this paper, the sequential backward elimination (SBE) method for feature selection is employed [32]. SBE is a wrapper method, which searches to find the combination of features that yield the greatest accuracy for a specific classifier. SBE initializes the feature space by utilizing all features then starts to remove features iteratively. This procedure is recursively repeated until a specified number of features have been selected.

The performance of three different classifiers is compared for different numbers of features, as selected by SBE: multi-class SVM, a popular baseline used in the literature, random forest [33]–[35] and extreme gradient boosting (xgboost) [36], two other classifiers have been recently reported to give good results. The performance for SVM was compared for three different kernels—linear, polynomial, and radial basis function (RBF)—among which the linear kernel was found to yield the best results. The model parameters for the xgboost and random forest classifiers were optimized using a grid search over two parameters: the number of trees in the forest and maximum depth of the tree. The best results were achieved for random forest with a 50 trees and a depth of 20, and for xgboost with 50 trees and a depth of 10.

After optimization of classifier parameters, performance was compared as a function of number of features,

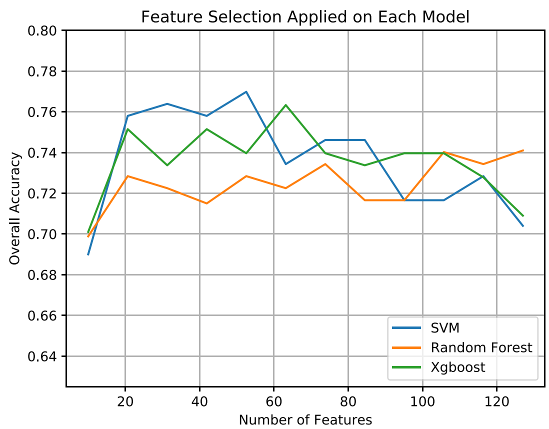

Fig. 4. Comparison of feature selection results for SVM, random forest and xgboost classifiers.

as shown in Fig. 4. The best performance was achieved by SVM with a linear kernel using 50 features selected with SBE; namely, the bandwidth of the torso response, mean torso frequency, mean of the upper envelope, mean of the lower envelope, first 2 CVD features, first 2 cepstral coefficients, 37 LPC coefficients, and 5 DCT features. The effect of feature selection is somewhat less apparent in random forest and xgboost classifiers, in part because tree-based models employ impurity-based feature rankings, implicitly providing for feature selection during training.

IV. DEEP LEARNING ARCHITECTURES

Deep learning is a method for machine learning that recently has experienced a resurgence due to the increased computing capabilities offered by modern GPU's and advances in algorithms. Deep neural networks build upon past research on artificial neural networks (ANNs) by increasing the overall size of the network using many layers of neurons. Each neuron is formed by linearly weighting multiple inputs supplied to an activation function. Formerly, it was common for sigmoid or hyperbolic tangent functions to be used for activation; however, network size was limited by what is known as the "vanishing gradient" problem. Neural networks are trained by using a gradient descent algorithm during backpropagation, which functions to minimize a predefined loss function. However, during backpropagation the error decreases as it flows through each layer, making training slow or even impossible as the number of layers increases. This problem was solved through the recent proposal of using rectified linear units (ReLU) as activation functions [37]. ReLU are mathematically defined as $f(x) = \max(0, x)$ and have an output of zero for negative input, but a linear output for positive input. By not squashing the data between 0 and 1, ReLU has been shown to prevent the vanishing gradient problem and has the additional advantage of enabling a sparse representation of the data when then network is initialized randomly [38]. In this way, ReLU units have enabled the design of modern-day "deep" networks yielding incredible performance gains in the classification of massive datasets.

In particular, CNN became popular when an eight-layer architecture, AlexNet [39], won the ImageNet Large-Scale Visual Recognition Challenge in 2012. Subsequently, a 16-layer CNN architecture, called VGG-Net [40], and a 152-layer architecture built by Microsoft called ResNet [41], won the competition in 2014 and 2016, respectively. Current research in deep learning involves processing over millions images or videos into thousands of classes.

This has led researchers in the radar community to also experiment with deep learning architectures to classify RF signals. However, a fundamental challenge in applying deep neural networks to RF signal classification is the limitation in dataset size. RF data measurements are much more difficult, time consuming, and costly to collect, especially for commercial ground surveillance radar systems. It is not practical to collect millions of radar micro-Doppler signatures and thus algorithms must be designed so as to avoid overfitting—the memorization of small datasets by high-complexity deep architectures. Thus, although a 14-layer deep CNN architecture has been recently proposed for human multitarget gait classification [42], the use of four-layers [43] or less has been more common. In this paper, we consider three-layer CNN and AE architectures for comparison with the proposed three-layer CAE architecture.

A. Autoencoder

An AE is a feed-forward neural network that aims to reconstruct the input at the output under certain constraints. In other words, for a given input vector of x, the AE tries to approximate $h_w(x) \approx x$. In 2006, an unsupervised pretraining algorithm was proposed for initializing the weights and biases of AE [44] that was highly effective when only a small number of labeled training samples were available [23], [45]. AE implement unsupervised pretraining by first encoding and then decoding the inputs.

For a given input vector x, the encoder computes a nonlinear mapping of the inputs as

$$e_i = \sigma(W x_i + b). \tag{7}$$

Here, σ denotes a nonlinear activation function, W denotes weights and b denotes the biases of the encoder. The encoded features are then decoded to reconstruct the given input vector x using

$$z_i = \sigma(\widetilde{W} e_i + \widetilde{b}). \tag{8}$$

Here, $\widetilde{W}$ and $\widetilde{b}$ denote weights and biases of the decoder. During unsupervised pretraining, the network tries to minimize the reconstruction error

$$J(\theta) = \frac{1}{N} \sum_{i=1}^{N} (x_i - z_i)^2 \tag{9}$$

by adjusting its weights and biases $\theta = [W, b, \widetilde{W}, \widetilde{b}]$. To prevent the network from learning the identity function, a sparsity parameter is added to the cost function. This parameter forces the network to learn the correlation between the given input vectors [46]. After adding the sparsity pa-

TABLE II
Parameter Optimization Table for AE (Acc. denotes accuracy)

Depth	Width	Acc. (%)	Depth	Width	Acc. (%)
1	20	74.1	4	20-50-100-200	83.4
1	50	76	4	40-100-200-400	83.1
1	100	75.5	4	100-200-400-800	79.8
2	20-50	79.8	5	20-50-100-200-400	82.7
2	50-100	81.1	5	40-100-200-400-800	82.8
2	100-200	80.9	5	100-200-400-800-1600	79.5
3	20-50-100	83.4	6	20-50-100-200-400-800	80.1
3	40-80-160	83.2	6	40-100-200-400-800-1600	78.9
3	**50-100-200**	**84.1**	6	100-200-400-800-1600-3200	78.3

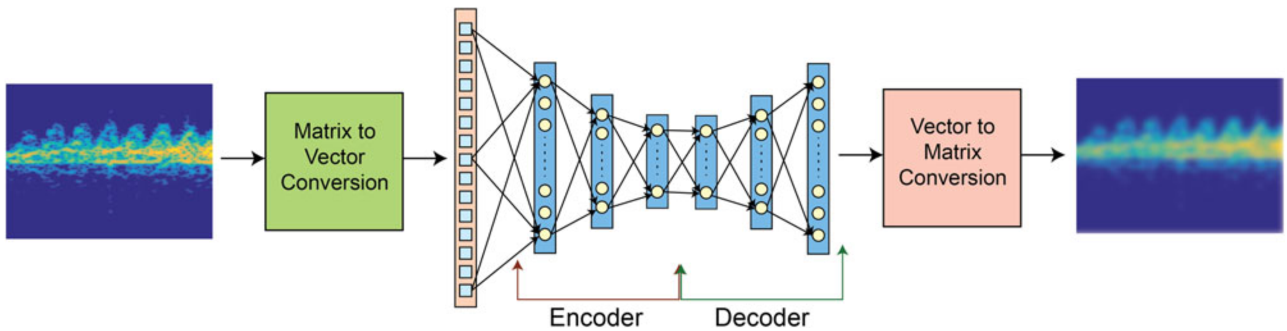

Fig. 5. Three-layer AE, where encoder layers have 200–100–50 neurons and decoder layers have 50–100–200 neurons.

rameter, the cost function, thus, becomes

$$\text{argmin}_\theta\ J(\theta) = \frac{1}{N}\sum_{i=1}^{N}(x_i - z_i)^2 + \beta\sum_{j=1}^{h} KL(p||p_j). \tag{10}$$

Here, h denotes the number of neurons in the hidden layer, β denotes sparsity proportion and $\sum_{j=1}^{h} KL(p||p_j)$ denotes the Kullback–Leibler (KL) divergence between the Bernoulli random variables with mean p and p_j, respectively. The KL divergence between two random variables is given as follows:

$$KL(p||p_j) = p\log\left(\frac{p}{p_j}\right) + (1-p)\log\left(\frac{1-p}{1-p_j}\right) \tag{11}$$

where p_j denotes the activation of jth neuron in the hidden layer and p is the desired average activation value. Since h is the number of neurons in the hidden layer, the KL divergence term forces hidden unit activations within the proximity of p.

After unsupervised pretraining, the decoder is removed from the network and the remaining encoder components are trained in a supervised manner by adding a softmax classifier with 12 neurons after the encoder. The softmax classifier is a multinomial version of logistic regression. For a given input x_i, the softmax function estimates the probability that $P(y_k|x_i)$ for $k = 1, 2, ..., K$, where K denotes the number of classes (12 in this case). In other words, the probability that the input x_i belongs to the class label y_k is estimated. Mathematically, the class probability p_k can be given as

$$p(y = k|x_i) = \frac{e^{\theta_k x_i}}{\sum_{k=1}^{K} e^{\theta_k x_i}}. \tag{12}$$

The weights and biases of the network, θ, can be optimized by minimizing the following cost function:

$$J(\theta) = -\sum_{i=1}^{N}\sum_{k=1}^{K} 1\{y^i = k\}\log\frac{e^{\theta_k x_i}}{\sum_{k=1}^{K} e^{\theta_k x_i}} \tag{13}$$

where 1{.} denotes the indicator function and N denotes the number of labeled samples. Equation (13) can be solved with a gradient-based algorithm. This process is called fine-tuning, where the network is being trained in supervised fashion. During fine tuning, instead of mean square error, categorical cross-entropy loss is selected as the loss function.

An AE can be stacked hierarchically such that upper layers receive inputs from the outputs of the layers below. A ReLU activation function is used for nonlinearity. KL divergence term for sparsity regularization is selected to be 2 and β is selected as 0.1. The optimization of both unsupervised pretraining and fine tuning is computed using the adaptive moment estimation (ADAM) [47] algorithm with a learning rate of 0.001. Using a grid search to determine the optimal depth and width without overfitting (summarized in Table II, with optimal parameters in bold), we chose to implement a three-layer autoencoder, with layers of 200–100–50 neurons, respectively. The overall AE architecture is shown in Fig. 5.

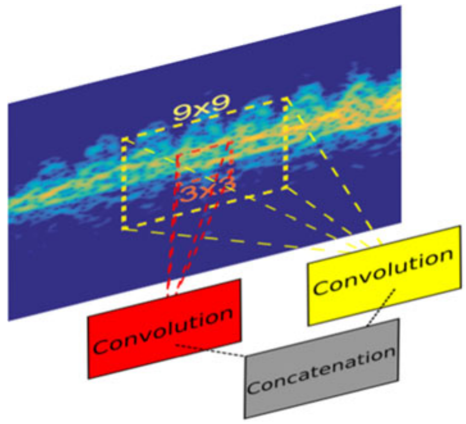

Fig. 6. Proposed filter concatenation for CNN and CAE.

B. Convolutional Neural Network (CNN)

CNNs have recently achieved great success in image classification due to their ability to learn locally connected features. CNNs generally consist of three elements: convolutional layers, pooling layers, and fully connected layers [48]. In the convolutional layer, filters are convolved with the receptive field of the input image in a sliding window style to learn data-specific features. Basic features, such as lines, edges, and corners, are learned in the initial layers, while more abstract features are learned as layers go deeper. For a given matrix P, mth neuron in the CNN calculates

$$M[i,\, j] = \sigma\left(\sum_{x=-2k-1}^{2k+1}\sum_{y=-2k-1}^{2k+1} f_m[x,\, y]P[i-x,\, j-y] + b\right) \tag{14}$$

where the origin is as defined being in the center of the image, so that the edge of the image is k-pixels from the origin pixel in either the direction of the x- or y-axis. Then, the size of each side of the image is $2k+1$, M is the activation map of the given input P, f_m is the mth convolution filter and σ is the nonlinear activation function. ReLU is used as the activation function.

Generally, a pooling layer follows each convolutional layer. Max-pooling is basically a nonlinear down-sampling procedure, which takes the maximum of 2×2 neighborhoods of the image, and helps to reduce the computational complexity for the forward layers, as well as adding translation invariancy to the network.

Fully connected layers are used to learn the nonlinear combinations of extracted features from previous layers. Dropout is recommended as a way of preventing overfitting by disabling randomly chosen neurons and their connections [49]. The dropped neurons stay inactive during the feedforward and backpropagation phases, thus forcing the network to learn different nonlinear combinations of features on each epoch.

In this paper, a filter concatenation technique is also applied to capture features of different resolutions from the input [24]. Two convolutional filters of different sizes are used. The larger filter captures more general features, while the smaller filter captures fine details. In this way, filter concatenation increases computational cost in return for improvement in classification performance. Fig. 6 illustrates the concept of filter concatenation.

In Table III, we compared the effect of filter size, as well as depth and width on the resulting accuracy. Based on this analysis, we chose filter sizes of 3×3 and 9×9 for concatenation, together with three convolutional layers using 30 3×3 filters (as highlighted in bold in Table III). After each convolutional layer, a 2×2 max pooling operation is applied. At the end of the network, the learned features are flattened to enable input to the fully connected layers. Two fully connected layers with 150 neurons in each layer are employed. After each fully connected layer, a dropout operation is applied with a probability of 0.5. Last, the network is connected to a softmax classifier with 12 inputs—the total number of classes. The same objective function given in (13) is optimized using ADAM. The CNN architecture is shown in Fig. 7.

C. Convolutional Autoencoder (CAE)

CAE combine the benefits of convolutional filtering in CNN's with unsupervised pretraining of AE. In contrast to the topology for AE, however, instead of the fully connected layers, the encoder contains convolutional layers and the decoder contains deconvolutional layers. Deconvolutional filters may be transposed versions of the convolutional filters; or, as is done in this paper, they may be learned from scratch. Additionally, each deconvolutional layer must be followed by an unpooling layer [50]. The unpooling operation is performed by storing the locations of the maximum values during pooling, preserving the values of these locations during unpooling, and zeroing the rest.

Spatial locality is preserved by incorporating a convolution operation at each neuron. Thus, for a given input maxrix P, the encoder computes

$$e_i = \sigma(P * F^n + b) \tag{15}$$

where σ denotes activation function, * represents 2-D convolution, F^n is nth 2-D convolutional filter, and b denotes encoder bias. To retain spatial resolution, zero padding is applied to the input matrix P. Then, the reconstruction can be obtained using

$$z_i = \sigma(e_i * \widetilde{F}^n + \widetilde{b}). \tag{16}$$

Here, z_i is the reconstruction of ith input $\widetilde{F}^n$ denotes nth 2-D convolutional filter in decoder and $\widetilde{b}$ is bias of decoder. Unsupervised pretraining can be applied to the network, which aims to minimize following equation:

$$E(\theta) = \sum_{i=1}^{m}(x_i - z_i)^2. \tag{17}$$

After unsupervised pretraining the unpooling and deconvolutional layers, the decoding part of the network is removed and fully connected layers as well as a softmax classifier are added at the end of the network. Then, the network can be fine-tuned by optimizing (13). As done

TABLE III
Parameter Optimization Table for CNN

Filter Size	Depth	Width	Acc(%)	Depth	Width	Acc(%)	Depth	Width	Acc(%)
3x3 - 9x9	1	5	80.2	3	5	88.4	5	5	87.2
	1	30	81.4	**3**	**30**	**90.1**	5	30	88.1
	1	100	81.5	3	100	90	5	100	88.4
	2	5	82.1	4	5	87.6	6	5	84.9
	2	30	86.2	4	30	89.9	6	30	85.5
	2	100	87.1	4	100	89.5	6	100	86.8
2x2 - 7x7	1	5	79.6	3	5	84.9	5	5	87.8
	1	30	80.4	3	30	88.8	5	30	88
	1	100	81.7	3	100	89.5	5	100	88.6
	2	5	83.4	4	5	86.9	6	5	85.3
	2	30	86.1	4	30	88.8	6	30	86.1
	2	100	87.6	4	100	89.3	6	100	86.2

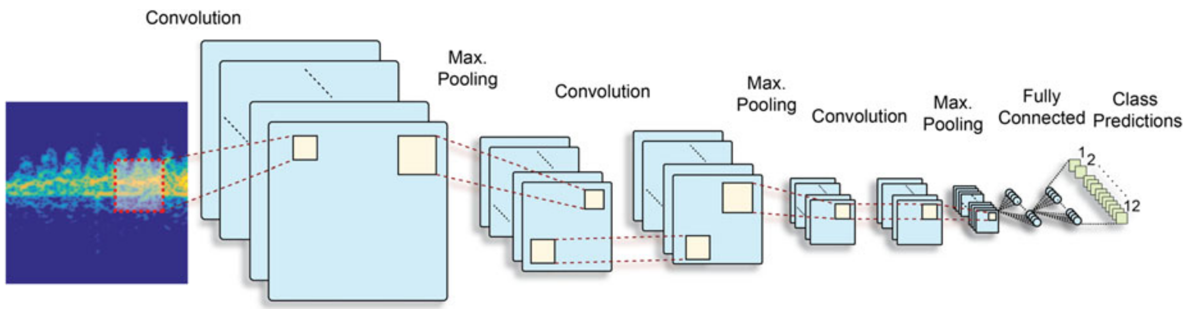

Fig. 7. CNN architecture implemented with three convolutional layers comprised of 30 3 $\times$ 3 filters each, and two fully connected layers with 150 neurons/layer.

with the CNN, a ReLU activation function is used, as well as the ADAM algorithm for optimization of the two fully connected layers with 150 neurons each, and dropout with a 0.5 probability on each fully connected layer.

The optimization of hyperparameters was done through grid search, as given in detail in Table IV, where optimal set is highlighted in bold. From these results, we chose to implement a CAE with three convolutional layers and populate the convolutional and deconvolutional layers with 30 3 $\times$ 3 and 9 $\times$ 9 concatenated filters. The overall structure of the proposed CAE is shown in Fig. 8.

V. RESULTS

A. Classification Accuracy

In this paper, deep learning models are implemented in Python using Keras [51], which uses Tensorflow as its tensor manipulation library [52]. All classifiers described in Sections III and IV are tested using tenfold cross validation of the 4 GHz continuous wave (CW) radar dataset described in Section II. Each deep learning architecture is trained for 280 epochs with a minibatch size of 100. The validation accuracy is computed by setting aside 20% of training samples as the validation set, and then evaluating the model after each epoch using the validation set.

To demonstrate the value of unsupervised pretraining, as offered by the proposed CAE, we compare two cases

1) Randomly initialization of the CNN.
2) Unsupervised pretraining over 20 epochs to initialize the proposed CAE.

In both cases, the learned weights are supplied as features to a multiclass SVM classifier and results are compared. We found that while random initialization of the CNN resulted in a classification accuracy of just 8.3%, the CAE using unsupervised pretraining achieved 83.4%—a drastically better result.

Of course, in the proposed approach we ultimately do not use just unsupervised pretraining, but additionally apply supervised fine-tuning and use a softmax classifier, instead of an SVM. Fig. 9 compares the variation of validation accuracy as a function of epoch for all three deep learning architectures considered. Notice that after just the first few epochs, the methods that employed unsupervised pretraining, namely AE and CAE, have much higher validation accuracies of 51% and 62%, respectively, in comparison to the roughly 31% performance of the CNN. During unsupervised pretraining the networks were trained for three epochs, yielding a mean square error of 0.01 and 0.5 for CAE and AE, respectively. The validation accuracy curves level off after about 75 epochs, and remain roughly constant thereafter, confirming that there is no overfitting in any of the deep architectures implemented.

Confusion matrices summarizing the classification accuracy of each technique are given in Tables V–VIII for multiclass SVM, AE, CNN, and the proposed CAE architecture (correct classification rates highlighted in bold), respectively, while precision and recall results for all methods are given in Table IX, where the highest classification accuracies are highlighted in bold. In these tables, green indicates classification accuracy, red denotes high error, i.e.,

TABLE IV
Parameter Optimization Table for CAE

Filter Size	Depth	Width	Acc(%)	Depth	Width	Acc(%)	Depth	Width	Acc(%)
3x3 - 9x9	1	5	83.8	3	5	92.2	5	5	93.2
	1	30	84.9	**3**	**30**	**94.2**	5	30	93.4
	1	100	84.7	3	100	93.2	5	100	93.9
	2	5	88.2	4	5	94	6	5	90.1
	2	30	88.4	4	30	94.1	6	30	90.9
	2	100	89	4	100	93.7	6	100	90.3
2x2 - 7x7	1	5	82.1	3	5	92.4	5	5	92.1
	1	30	84.4	3	30	93.9	5	30	92.9
	1	100	84.5	3	100	93.8	5	100	91.2
	2	5	88	4	5	92.8	6	5	89.8
	2	30	88.5	4	30	93.2	6	30	90.5
	2	100	88.6	4	100	92.9	6	100	90.3

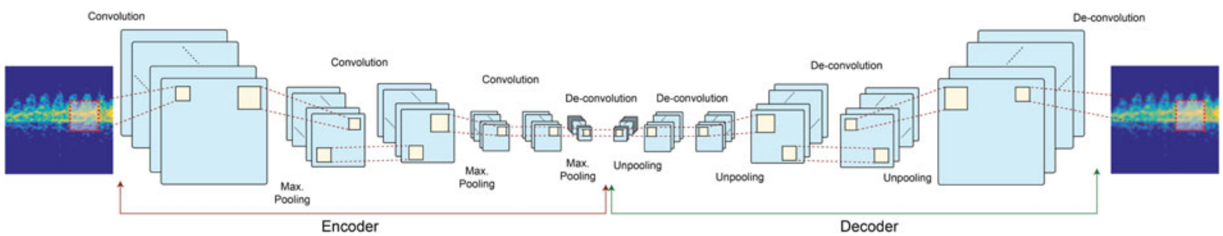

Fig. 8. Proposed CAE architecture showing convolutional and deconvolutional layers. After unsupervised pretraining the decoder part is removed and two fully connected layers and a softmax classifier are added at the end of encoder.

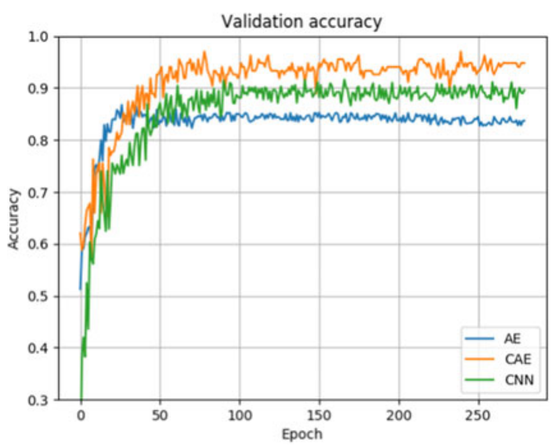

Fig. 9. Comparison of validation accuracies for AE, CNN, and CAE.

>20% confusion, brown denotes errors between 10% and 20%, and last, yellow denotes errors lower than 10%. These results show that the performance of DNNs are between 7% and 17% higher than that achieved using a select set of predefined features supplied to multiclass SVM. This is a significant result as it shows the clear benefits of learning features directly from the data, especially in cases when the classes being considered are highly similar and visual difference between micro-Doppler signatures are minimal.

Among deep learning architectures, the proposed CAE architecture surpasses the performance attained with the CNN or AE. An overall classification accuracy of 94.2% was achieved with the CAE, while the CNN and AE yielded classification accuracies of 90.1% and 84.1%, respectively. This represents a 4%–10% improvement in performance, primarily due to the exploitation of unsupervised pretraining together with the benefits of spatially localized processing offered by convolutional filtering and filter concatenation.

B. Discussion of Classification Results

The AE exhibited significant confusions between some inherently similar classes, namely

1) using a cane with limping and using a walker;
2) falling with falling off of a chair and sitting; and
3) crawling with creeping.

while the confusion of crawling with jogging was more surprising. The CNN was able to distinguish falling off a chair and sitting, but the confusion between falling forward and falling of a chair was significantly higher. Moreover, the confusion between limping and using a walker, and using a cane; as well as using crutches, creeping, crawling, and jogging was more evident. In contrast, the proposed CAE architecture had no problems differentiating falling forward from falling off a chair, while some amount of confusion between limping-cane, cane-walker, and creeping-crawling remained. The CAE did confuse falling and sitting for 9.4% of the relevant samples, but the confusion between creeping and crawling was reduced by 8.4%. Creeping is seen to have the highest in class variance due to difficulty of subjects in advancing forward on the stomach without rising upon their knees and elbows—an act that increases similarity with crawling. Moreover, the confusion in creeping also reflects the difficulty in generalizing an activity that is not consistent. Overall, the proposed CAE architecture outperformed the multiclass SVM, CNN, and AE architectures for all activity classes, except creeping and falling, for which case the difference was under 1%.

TABLE V
Confusion Matrix for Multiclass SVM and 50 Selected Features (Overall Accuracy is 76.9%)

%	Walking	Wheelchair	Limping	Cane	Walker	Falling	Crutches	Creeping	Crawling	Jogging	Sitting	F.C
Walking	**100**	0	0	0	0	0	0	0	0	0	0	0
Wheelchair	0	**83.9**	3.2	12.9	0	0	0	0	0	0	0	0
Limping	0	0	**72.4**	15.6	12	0	0	0	0	0	0	0
Cane	0	3.8	0	**76.9**	19.3	0	0	0	0	0	0	0
Walker	0	4.4	0	8.7	**86.9**	0	0	0	0	0	0	0
Falling	25	0	0	0	0	**55**	0	0	0	0	0	20
Crutches	0	0	0	0	0	0	**100**	0	0	0	0	0
Creeping	50	0	0	0	0	0	0	**37.5**	12.5	0	0	0
Crawling	0	14.3	0	0	0	0	0	43.1	**28.3**	14.3	0	0
Jogging	0	0	0	0	0	0	0	0	0	**95.7**	0	4.3
Sitting	0	0	0	0	0	0	0	0	0	0	**100**	0
F.C	0	0	0	0	0	0	0	0	0	0	14.3	**85.7**

TABLE VI
Confusion Matrix for Autoencoder (Overall Accuracy is 84.1%)

%	Walking	Wheelchair	Limping	Cane	Walker	Falling	Crutches	Creeping	Crawling	Jogging	Sitting	F.C
Walking	**91.1**	0	0	0	0	0	0	8.9	0	0	0	0
Wheelchair	0	**91.4**	2.9	0	4.1	0	0	1.6	0	0	0	0
Limping	0	0	**84.4**	7.3	8.3	0	0	0	0	0	0	0
Cane	0	0	10.1	**69.1**	20.8	0	0	0	0	0	0	0
Walker	0	0.1	0.1	9.1	**90.7**	0	0	0	0	0	0	0
Falling	0.5	0	0	0	0	**89.3**	0	0	0	0	0	10.2
Crutches	7	0	0	0	0	0	**91.5**	0	1.5	0	0	0
Creeping	0	0	0	0	0	0	0	**70.4**	29.6	0	0	0
Crawling	2.1	0	0	0	0	0	0	24.5	**60.9**	12.5	0	0
Jogging	0.4	0	0	0	0	0	0	0	0	**98.1**	0	1.5
Sitting	0	0	0	0	0	19.6	0	0	0	0	**80.4**	0
F.C	0	0	0	0	0	8.5	0	0	0	0	0	**91.5**

TABLE VII
Confusion Matrix for CNN (Overall Accuracy is 90.1%)

%	Walking	Wheelchair	Limping	Cane	Walker	Falling	Crutches	Creeping	Crawling	Jogging	Sitting	F.C
Walking	**100**	0	0	0	0	0	0	0	0	0	0	0
Wheelchair	0	**100**	0	0	0	0	0	0	0	0	0	0
Limping	0	0	**86.2**	13.8	0	0	0	0	0	0	0	0
Cane	0	0	3.9	**81.9**	14.2	0	0	0	0	0	0	0
Walker	0	0	0	10.3	**89.7**	0	0	0	0	0	0	0
Falling	0	0	0	0	0	**86.4**	0	0	0	0	0	13.6
Crutches	0	0	0	0	0	0	**100**	0	0	0	0	0
Creeping	0	0	0	0	0	0	10.3	**51.2**	30.8	7.7	0	0
Crawling	0	0	0	0	0	0	0	0	**85.7**	14.3	0	0
Jogging	0	0	0	0	0	0	0	0	0	**100**	0	0
Sitting	0	0	0	0	0	0	0	0	0	0	**100**	0
F.C	0	0	0	0	0	0	0	0	0	0	0	**100**

TABLE VIII
Confusion Matrix for Convolutional Autoencoder (Overall Accuracy is 94.2%)

%	Walking	Wheelchair	Limping	Cane	Walker	Falling	Crutches	Creeping	Crawling	Jogging	Sitting	F.C
Walking	**100**	0	0	0	0	0	0	0	0	0	0	0
Wheelchair	0	**100**	0	0	0	0	0	0	0	0	0	0
Limping	0	0	**93.1**	6.9	0	0	0	0	0	0	0	0
Cane	0	0	0	**91.1**	8.9	0	0	0	0	0	0	0
Walker	0	0	0	0	**100**	0	0	0	0	0	0	0
Falling	0	0	0	0	0	**89**	0	0	0	0	9.4	1.6
Crutches	0	0	0	0	0	0	**100**	0	0	0	0	0
Creeping	4.9	0	0	0	0	0	7.2	**65.5**	22.4	0	0	0
Crawling	0	0	0	0	0	0	0	8.5	**91.5**	0	0	0
Jogging	0	0	0	0	0	0	0	0	0	**100**	0	0
Sitting	0	0	0	0	0	0	0	0	0	0	**100**	0
F.C	0	0	0	0	0	0	0	0	0	0	0	**100**

C. Computational Complexity

A comparison of computation time and number of network parameters is given in Table X. These numbers are based on running all deep learning networks on a system with the following specifications: NVIDIA Tesla K80 GPU with 24 GB of VRAM, 378 GB of ram and Intel Xeon E5 2683 processor. Utilization of the GPU accelerates computations by a factor of ten (approximately) and is essential for deep learning implementations. In contrast, conventional methods using predefined features are much faster and less complex, therefore, GPUs are not required and training on

TABLE IX
Precision (P), Recall (R), and Accuracy (A) Values for all Methods

Gait	SVM w/F.S. P	SVM w/F.S. R	SVM w/F.S. A	AE P	AE R	AE A	CNN P	CNN R	CNN A	CAE P	CAE R	CAE A
Walking	1	0.57	**100**	0.91	0.9	91.1	1	1	**100**	1	0.95	**100**
Wheel chair	0.84	0.79	83.9	0.91	1	91.4	1	1	**100**	1	1	**100**
Limping	0.72	0.96	72.4	0.84	0.87	84.4	0.86	0.96	86.2	0.93	1	**93.1**
Cane	0.77	0.67	76.9	0.69	0.81	69.1	0.82	0.77	81.9	0.91	0.93	**91.1**
Walker	0.87	0.74	86.9	0.91	0.73	90.7	0.9	0.86	89.7	1	0.92	**100**
Falling	0.55	1	55	0.89	0.76	**89.3**	0.86	1	86.4	0.89	1	89
Crutches	1	1	**100**	0.92	1	91.5	1	0.91	**100**	1	0.93	**100**
Creeping	0.38	0.47	37.5	0.7	0.67	**70.4**	0.51	1	51.2	0.66	0.89	65.5
Crawling	0.28	0.69	28.3	0.61	0.66	60.9	0.86	0.74	85.7	0.92	0.8	**91.5**
Jogging	0.96	0.87	95.7	0.98	0.89	98.1	1	0.82	**100**	1	1	**100**
Fastly Sitting	1	0.87	**100**	0.8	1	80.4	1	1	**100**	1	0.91	**100**
Falling from Chair	0.86	0.78	85.7	0.92	0.89	91.5	1	0.88	**100**	1	0.98	**100**
Average	0.77	0.78	76.9	0.84	0.85	84.1	0.9	0.91	90.1	**0.94**	**0.94**	**94.2**

TABLE X
Computational Complexity for all Methods (F.S. Denotes Feature Selection and F.C. Denotes Filter Concatenation)

	SVM	SVM w/F.S.	AE	CNN	CNN w/F.C.	CAE	CAE w/F.C
Total Params.	-	-	6.361.562	832.428	1.980.324	832.428	1.980.324
Conv. Params.	-	-	-	18.816	371.712	18.816	371.712
Total Time	37 s.	99 s.	943 s.	157 s.	463 s.	241 s.	747 s.

a CPU is feasible. The 37 s duration reported for SVM involves both feature extraction and classifier training. In general, the computation time will depend on the numbers of features to be selected. Results are shown for 50 features.

In contrast, deep learning algorithms require vast amounts of computational resources. The convolutional operations used by the CNN and CAE add complexity relative to the computations done by a single neuron in the autoencoder; however, all of the AE neurons are fully connected, resulting in actually the greatest number of parameters, and hence, longest training time. The filter concatenation technique, which improves accuracy, also comes with a computational cost, reflected in greatly increasing the number of convolutional parameters and more than doubling the total number of parameters in the network. Unsupervised pretraining likewise improves performance but adds to the total training time required.

D. Discussion of Deep Learning of Features

One way of getting a better understanding of how the propsed CAE architecture better learns features is to visualize the convolutional filters of each layer. To do this, the activation maximization technique [53] was employed, which works by modifying a randomly generated image such that the activation of a selected filter is maximized. Mathematically, this can be achieved by maximizing the following loss function:

$$x_d = \underset{x}{\operatorname{argmax}}(h_{ik}(\theta, x)) \tag{18}$$

where x is the randomly generated input image, θ are the weights and biases of the network and h_{ik} is the activation of the kth filter in the ith layer. The variable x_d is the desired result, i.e., the image yields highest activation for h_{ik}. This optimization problem can be solved by using the gradient ascent algorithm

$$x = x + \alpha \frac{\partial(h_{ik}(\theta, x))}{\partial x} \tag{19}$$

where α is the step size. The gradient $\frac{\partial(h_{ik}(\theta,x))}{\partial x}$ yields the direction in which to update the input image x in order to have the highest activation for h_{ik}. Fig. 8 shows first 25 filters that have obtained by computing (19) for 20 steps with $\alpha = 0.8$. The filters shown in Fig. 9 have the highest loss according to (18).

From Fig. 10 it can be seen that the network is learning to extract basic orientations on the first layer: the 9×9 filters (top three rows) learn more generalized shapes, whereas the 3×3 filters (bottom two rows) learn more specific shapes. As the layers go deeper, the second and third layers learn more abstract shapes, as can be seen by the clear horizontal lines of the third filter in the first row of Layer 2 and the fourth filter in the first row of Layer 3.

Also, it may be observed that some filters have learned clutter and noise. This is significant because in this paper no clutter cancellation or clutter filtering has been applied to remove ground clutter, visible as a narrow band near 0 Hz Doppler frequency. In fact, past work has shown that clutter has a significant affect on classifier performance when predefined features are used, so that clutter filtering is typically beneficial [54]. But, in the case of deep learning architectures, and, in particular, the proposed CAE, the clutter is separated in the convolutional filtering process and effectively discarded during the learning process. Thus, the deep learning architectures are not sensitive to the affects of ground clutter, caused by furniture (tables and bookshelves) present in the indoor laboratory environment—yet another

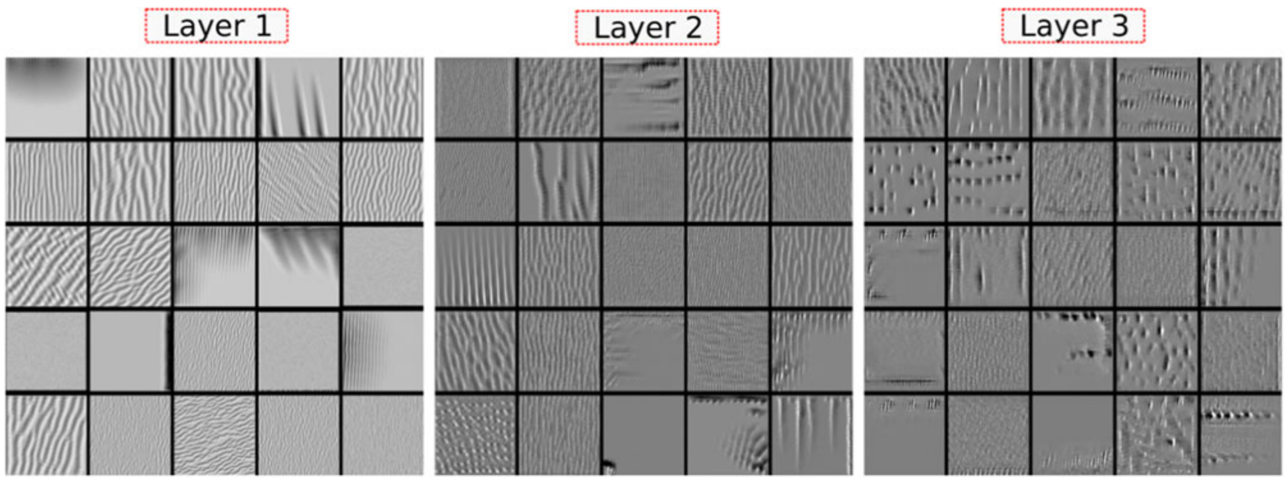

Fig. 10. Visualization of learned filters for CAE model, 25 of 64 filters are shown for each layer with the 9×9 filters in the top three rows and the 3×3 filters in the bottom two rows.

advantage of learning features in contrast to extracting predefined features.

VI. CONCLUSION

This paper shows that a CAE architecture that takes advantage of both unsupervised pretraining as well as the localized spatial features enabled by convolutional filtering outperforms other deep architectures such as CNN, autoencoder, as well as multiclass SVM taking predefined features. While the performance gain over other deep learning architectures is 4.1% and 10.1%, for CNN and AE, respectively, the improvement over multiclass SVM is 17.3%. These results clearly show the advantage of deep learning, especially in the cases when the classes are highly similar. Moreover, inspection of the filters in each layer reveals that deep learning architectures can also separate components due to clutter and noise, eliminating the need for explicit ground clutter cancellation, or filtering prior to classification. The high classification accuracy of 94.2% for discriminating 12 indoor activity classes involving aided and unaided human motion also shows the potential for using radar-based health monitoring systems for assisted living. Future work will involve estimation of gait parameters when walking is detected for the purposes of fall risk assessment and neuromuscular disease monitoring.

ACKNOWLEDGMENT

The authors would like to thank A. Serinöz and E. P. Altıner for their contributions in creating the dataset.

REFERENCES

[1] S. Z. Gürbüz, Ü. Kaynak, B. Özkan, O. C. Kocaman, F. Kıyıcı, and B. Tekeli
Design study of a short-range airborne uav radar for human monitoring
In *Proc. IEEE 48th Asilomar Conf. Signals, Syst. Comput.*, 2014, pp. 568–572.

[2] F. Fioranelli, M. Ritchie, and H. Griffiths
Classification of unarmed/armed personnel using the netrad multistatic radar for micro-doppler and singular value decomposition features
IEEE Geoscience Remote Sensing Lett., vol. 12, no. 9, pp. 1933–1937, Sep. 2015.

[3] P. Khomchuk, I. Stainvas, and I. Bilik
Pedestrian motion direction estimation using simulated automotive mimo radar
IEEE Trans. Aerosp, Electron. Syst., vol. 52, no. 3, pp. 1132–1145, Jun. 2016.

[4] M. G. Amin, Y. D. Zhang, F. Ahmad, and K. D. Ho
Radar signal processing for elderly fall detection: The future for in-home monitoring
IEEE Signal Process. Mag., vol. 33, no. 2, pp. 71–80, Mar. 2016.

[5] C. Garripoli *et al.*
Embedded dSP-based telehealth radar system for remote indoor fall detection
IEEE J. Biomed. Health Informat., vol. 19, no. 1, pp. 92–101, Jan. 2015.

[6] B. Y. Su, K. Ho, M. J. Rantz, and M. Skubic
Doppler radar fall activity detection using the wavelet transform
IEEE Trans. Biomed. Eng., vol. 62, no. 3, pp. 865–875, Mar. 2015.

[7] Q. Wu, Y. D. Zhang, W. Tao, and M. G. Amin
Radar-based fall detection based on doppler time–frequency signatures for assisted living
IET Radar, Sonar Navig., vol. 9, no. 2, pp. 164–172, 2015.

[8] S. Z. Gürbüz, B. Erol, B. Çağlıyan, and B. Tekeli
Operational assessment and adaptive selection of micro-doppler features
IET Radar, Sonar Navig., vol. 9, no. 9, pp. 1196–1204, 2015.

[9] Y. Kim, S. Ha, and J. Kwon
Human detection using doppler radar based on physical characteristics of targets
IEEE Geosci. Remote Sens. Lett., vol. 12, no. 2, pp. 289–293, Feb. 2015.

[10] P. Molchanov, J. Astola, K. Egiazarian, and A. Totsky
Ground moving target classification by using dct coefficients extracted from micro-doppler radar signatures and artificial neuron network
In *Proc. Microw. Radar Remote Sens. Symp.*, 2011, pp. 173–176.

[11] D. Yessad, A. Amrouche, M. Debyeche, and M. Djeddou
Micro-doppler classification for ground surveillance radar using speech recognition tools
In *Proc. Iberoamer. Congr. Pattern Recognit.*, Springer, 2011, pp. 280–287.

[12] R. J. Javier and Y. Kim
Application of linear predictive coding for human activity classification based on micro-doppler signatures
IEEE Geosci. Remote Sens. Lett., vol. 11, no. 10, pp. 1831–1834, Oct. 2014.

[13] B. Tekeli, S. Z. Gurbuz, and M. Yuksel
Information-theoretic feature selection for human micro-doppler signature classification
IEEE Trans. Geosci. Remote Sens., vol. 54, no. 5, pp. 2749–2762, May. 2016.

[14] S. Z. Gurbuz, B. Tekeli, C. Karabacak, and M. Yuksel
Feature selection for classification of human micro-doppler
In *Proc. IEEE Int. Conf. Microw., Commun., Antennas Electron. Syst.,* 2013, pp. 1–5.

[15] J. Zabalza, C. Clemente, G. Di Caterina, J. Ren, J. J. Soraghan, and S. Marshall
Robust pca micro-doppler classification using svm on embedded systems
IEEE Trans. Aerosp. Electron. Syst., vol. 50, no. 3, pp. 2304–2310, Jul. 2014.

[16] Y. Kim and H. Ling
Human activity classification based on micro-doppler signatures using a support vector machine
IEEE Trans. Geosc. Remote Sens., vol. 47, no. 5, pp. 1328–1337, May 2009.

[17] M. S. Seyfioglu, S. Z. Gurbuz, M. Ozbayoglu, and M. Yuksel
Deep learning of micro-doppler features for aided and unaided gait recognition
In *Proc. IEEE Radar Conf.*, May 2017, pp. 1125–1130.

[18] Y. Kim and T. Moon
Human detection and activity classification based on micro-doppler signatures using deep convolutional neural networks
IEEE Geosc. Remote Sens. Lett., vol. 13, no. 1, pp. 8–12, Jan. 2016.

[19] B. Jokanovic, M. Amin, and F. Ahmad
Radar fall motion detection using deep learning
In *Proc. IEEE Radar Conf.,* 2016, pp. 1–6.

[20] D. Erhan, Y. Bengio, A. Courville, P.-A. Manzagol, P. Vincent, and S. Bengio
Why does unsupervised pre-training help deep learning?"
J. Mach. Learning Res., vol. 11, no. Feb, pp. 625–660, 2010.

[21] J. Masci, U. Meier, D. Cireşan, and J. Schmidhuber
Stacked convolutional auto-encoders for hierarchical feature extraction
Artif. Neural Netw. Mach. Learning, pp. 52–59, 2011.

[22] D. Erhan, Y. Bengio, A. Courville, P.-A. Manzagol, P. Vincent, and S. Bengio
Why does unsupervised pre-training help deep learning?"
J. Mach. Learn. Res., vol. 11, pp. 625–660, Mar. 2010. [Online]. Available: http://dl.acm.org/citation.cfm?id=1756006.1756025

[23] O. E. David and N. S. Netanyahu
Deeppainter: Painter classification using deep convolutional autoencoders
In *Proc. Int. Conf. Artif. Neural Netw.*, Springer, 2016, pp. 20–28.

[24] C. Szegedy *et al.*
Going deeper with convolutions
In *Proc. IEEE Conf. Comput. Vis. Pattern Recognit.*, 2015, pp. 1–9.

[25] N. V. Chawla, K. W. Bowyer, L. O. Hall, and W. P. Kegelmeyer
Smote: synthetic minority over-sampling technique
J. Artifi. Intell. Res., vol. 16, pp. 321–357, 2002.

[26] T. D. Bufler and R. M. Narayanan
Radar classification of indoor targets using support vector machines
IET Radar, Sonar Navig., vol. 10, no. 8, pp. 1468–1476, 2016.

[27] M. Otero
Application of a continuous wave radar for human gait recognition
In *Defense and Security.*, International Society for Optics and Photonics, 2005, pp. 538–548.

[28] S. Björklund, T. Johansson, and H. Petersson
Evaluation of a micro-doppler classification method on mm-wave data
In *Proc. 2012 IEEE Radar Conf.*, May 2012, pp. 0934–0939.

[29] C. Clemente, L. Pallotta, A. De Maio, J. J. Soraghan, and A. Farina
A novel algorithm for radar classification based on doppler characteristics exploiting orthogonal pseudo-zernike polynomials
IEEE Trans. Aerosp. Electron. Syst., vol. 51, no. 1, pp. 417–430, 2015.

[30] J. Zabalza
et al. Robust pca micro-doppler classification using svm on embedded systems
IEEE Trans. Aerosp. Electron. Syst., vol. 50, no. 3, pp. 2304–2310, Jul. 2014.

[31] F. Fioranelli, M. Ritchie, S. Z. Gurbuz, and H. Griffiths
Feature diversity for optimized human micro-doppler classification using multistatic radar
IEEE Trans. Aerosp. Electron. Syst., vol. 53, no. 2, pp. 640–654, Apr. 2017.

[32] Y. Saeys, I. Inza, and P. Larrañaga
A review of feature selection techniques in bioinformatics
bioinformatics, vol. 23, no. 19, pp. 2507–2517, 2007.

[33] M. Ritchie, M. Ash, Q. Chen, and K. Chetty
Through wall radar classification of human micro-doppler using singular value decomposition analysis
Sensors, vol. 16, no. 9, p. 1401, 2016.

[34] I. Rosa *et al.*
Classification success of six machine learning algorithms in radar ornithology
In *Proc. IBIS Int. J. Avian Sci.*, vol. 158, no. 1, pp. 28–42, Jan. 2016.

[35] S. Gurbuz, M. Seyfioglu, and F. Liechti
Identification of biological signals with radar
Short Term Scientific Mission Report, Oct. 2015. [Online]. Available: http://www.enram.eu/wp-content/uploads/2014/02/Vogelwarte_Gurbuz_STSM_O ctober2015_REPORT.pdf

[36] T. Chen and C. Guestrin
Xgboost: A scalable tree boosting system
In *Proc. 22nd ACM Int. Conf. Knowl. Discov. Data Mining.*, 2016, pp. 785–794.

[37] V. Nair and G. E. Hinton
Rectified linear units improve restricted boltzmann machines
In *Proc. 27th Int. Conf. Mach. Learning*, 2010, pp. 807–814.

[38] Y. Ioannou *et al.*
Decision forests, convolutional networks and the models in-between
Microsoft Research Tech. Rep. MSR-TR-2015-58, 2015.

[39] A. Krizhevsky, I. Sutskever, and G. E. Hinton
Imagenet classification with deep convolutional neural networks
In *Proc. Adv. Neural Inform. Process. Syst.*, 2012, pp. 1097–1105.

[40] K. Simonyan and A. Zisserman
Very deep convolutional networks for large-scale image recognition
In *Proc. 3rd Int. Conf. Learning Representations*, San Diego, 2015.

[41] K. He, X. Zhang, S. Ren, and J. Sun
Deep residual learning for image recognition
In *Proc. IEEE Conf. Comput. Vis. Pattern Recognit.*, 2016,

pp. 770–778.
[42] R. Trommel, R. Harmanny, L. Cifola, and J. Driessen
Multi-target human gait classification using deep convolutional neural networks on micro-doppler spectrograms
In *Proc. Radar Conf.*, 2016, pp. 81–84.
[43] Y. Kim and B. Toomajian
Hand gesture recognition using micro-doppler signatures with convolutional neural network
IEEE Access, vol. 4, pp. 7125–7130, 2016.
[44] G. E. Hinton and R. R. Salakhutdinov
Reducing the dimensionality of data with neural networks
Science, vol. 313, no. 5786, pp. 504–507, 2006.
[45] Y. Bengio, A. Courville, and P. Vincent
Representation learning: A review and new perspectives
IEEE Trans. Pattern Anal. Mach. Intell., vol. 35, no. 8, pp. 1798–1828, Aug. 2013.
[46] A. Ng
Sparse autoencoder
CS294A Lecture Notes, vol. 72, no. 2011, pp. 1–19, 2011.
[47] D. Kingma and J. Ba
Adam: A method for stochastic optimization
In *Proc. 3rd Int. Conf. Learning Representations*, San Diego, 2015.
[48] Y. LeCun *et al.*
Handwritten digit recognition with a back-propagation network
In *Proc. Adv. Neural Inform. Process. Syst. 2,*. Morgan Kaufmann, 1990, pp. 396–404.
[49] N. Srivastava, G. E. Hinton, A. Krizhevsky, I. Sutskever, and R. Salakhutdinov
Dropout: a simple way to prevent neural networks from overfitting
J. Mach. Learn. Res., vol. 15, no. 1, pp. 1929–1958, 2014.
[50] M. D. Zeiler, G. W. Taylor, and R. Fergus
Adaptive deconvolutional networks for mid and high level feature learning
In *Proc. IEEE Int. Conf. Comput. Vis.*, 2011, pp. 2018–2025.
[51] F. Chollet
Keras, 2015. [Online]. Available: https://github.com/fchollet/keras.
[52] M. Abadi
Tensorflow: Large-scale machine learning on heterogeneous distributed systems
arXiv preprint arXiv:1603.04467, 2016.
[53] D. Erhan, Y. Bengio, A. Courville, and P. Vincent
Visualizing higher-layer features of a deep network
Univ. Montreal, Montréal, Canada, vol. 1341, p. 3, Tech. Rep. 1341, 2009.
[54] B. Çağlıyan and S. Z. Gürbüz
Micro-doppler-based human activity classification using the mote-scale bumblebee radar
IEEE Geosci. Remote Sens. Lett., vol. 12, no. 10, pp. 2135–2139, Oct. 2015.

Mehmet Saygın Seyfioğlu received the B.S. and the M.S. degrees in electrical and electronics engineering from TOBB University of Economics and Technology (TOBB ETU), Ankara, Turkey, in May 2015 and December 2017, respectively.

From May 2015 to December 2016, he was a Teaching Assistant with TOBB ETU for a variety of classes relating to signal processing and communications. He is currently working with STM Defense Technologies Engineering and Trade Inc. as a Data Scientist. His research interests include deep learning, computer vision, and signal processing for radar and remote sensing.

Ahmet Murat Özbayoğlu received the B.S. degree from the Department of Electrical Engineering, Middle East Technical University, Ankara, Turkey, in 1991, with an emphasis on telecommunications and computers, and the M.S. and Ph.D. degrees in systems engineering from the Missouri University of Science and Technology, Rolla, MO, USA, in 1993 and 1996, respectively.

He was a Product Development Engineer and a Consultant with Beyond Inc., St. Peters, MO, USA. In 2001, he joined MEMC Electronic Materials Inc., Maryland Heights, MO, USA, as a Software Project Engineer, a Programmer, and an Analyst. In 2005, he joined the Department of Computer Engineering, TOBB University of Economics and Technology, Ankara. His current research interests include machine learning, pattern recognition, big data, computational intelligence, and machine vision.

Sevgi Z. Gürbüz (S'01–M'10–SM'17) received the B.S. degree in electrical engineering with minor in mechanical engineering and the M.Eng. degree in electrical engineering and computer science from the Massachusetts Institute of Technology, Cambridge, MA, USA, in 1998 and 2000, respectively, and the Ph.D. degree in electrical and computer engineering from Georgia Institute of Technology, Atlanta, GA, USA, in 2009.

From February 2000 to January 2004, she worked as a Radar Signal Processing Research Engineer with the U.S. Air Force Research Laboratory, Sensors Directorate, Rome, NY, USA. Formerly holding academic positions with the TOBB University of Economics and Technology in Ankara, Turkey and Utah State University, Logan, UT, USA, she is currently an Assistant Professor with the Department of Electrical and Computer Engineering, University of Alabama, Tuscaloosa, AL, USA. Her current research interests include radar signal processing, machine learning and pattern recognition, cognitive radar, and remote sensing.

Dr. Gurbuz is a recipient of a USAF Achievement Medal, USAF Commendation Medal, AFRL Technical Achievement Award, C.S. Draper Fellowship, National Defense Science and Engineering Fellowship, EU Marie Curie Research Fellowship, and the 2010 IEEE Radar Conference Best Student Paper Award.